AGU PUBLICATIONS

JGR

Journal of Geophysical Research: Oceans

RESEARCH ARTICLE

10.1002/2015JC010914

Influence of ice thickness and surface properties on light transmission through Arctic sea ice

Christian Katlein[1,2], Stefanie Arndt[1], Marcel Nicolaus[1], Donald K. Perovich[3], Michael V. Jakuba[4], Stefano Suman[4], Stephen Elliott[4], Louis L. Whitcomb[4,5], Christopher J. McFarland[5], Rüdiger Gerdes[1,2], Antje Boetius[1,6], and Christopher R. German[4]

[1]Alfred-Wegener-Institut Helmholtz-Zentrum für Polar- und Meeresforschung, Bremerhaven, Germany, [2]Jacobs University, Bremen, Germany, [3]Cold Regions Research and Engineering Laboratory, Hanover, New Hampshire, USA, [4]Woods Hole Oceanographic Institution, Deep Submergence Laboratory, Woods Hole, Massachusetts, USA, [5]Johns Hopkins University, Department of Mechanical Engineering, Baltimore, Maryland, USA, [6]Max Planck Institute for Marine Microbiology, Bremen, Germany

Key Points:
- Surface properties of sea ice strongly influence the light field on local scales
- Large scale variability of under ice light is determined by ice thickness
- Light transmittance can be inferred from thickness and albedo distribution

Correspondence to:
C. Katlein,
Christian.Katlein@awi.de

Citation:
Katlein, C., et al. (2015), Influence of ice thickness and surface properties on light transmission through Arctic sea ice, *J. Geophys. Res. Oceans*, *120*, 5932–5944, doi:10.1002/2015JC010914.

Received 18 APR 2015
Accepted 27 JUL 2015
Accepted article online 30 JUL 2015
Published online 4 SEP 2015

Abstract The observed changes in physical properties of sea ice such as decreased thickness and increased melt pond cover severely impact the energy budget of Arctic sea ice. Increased light transmission leads to increased deposition of solar energy in the upper ocean and thus plays a crucial role for amount and timing of sea-ice-melt and under-ice primary production. Recent developments in underwater technology provide new opportunities to study light transmission below the largely inaccessible underside of sea ice. We measured spectral under-ice radiance and irradiance using the new Nereid Under-Ice (NUI) underwater robotic vehicle, during a cruise of the R/V Polarstern to 83°N 6°W in the Arctic Ocean in July 2014. NUI is a next generation hybrid remotely operated vehicle (H-ROV) designed for both remotely piloted and autonomous surveys underneath land-fast and moving sea ice. Here we present results from one of the first comprehensive scientific dives of NUI employing its interdisciplinary sensor suite. We combine under-ice optical measurements with three dimensional under-ice topography (multibeam sonar) and aerial images of the surface conditions. We investigate the influence of spatially varying ice-thickness and surface properties on the spatial variability of light transmittance during summer. Our results show that surface properties such as melt ponds dominate the spatial distribution of the under-ice light field on small scales (<1000 m^2), while sea ice-thickness is the most important predictor for light transmission on larger scales. In addition, we propose the use of an algorithm to obtain histograms of light transmission from distributions of sea ice thickness and surface albedo.

1. Introduction

The sea ice cover of the Arctic Ocean has significantly decreased in the last decades [*Meier et al*., 2014; *Perovich*, 2011] by extent [*Serreze et al*., 2007; *Stroeve et al*., 2007, 2012] and in thickness [*Haas et al*., 2008; *Kwok and Rothrock*, 2009; *Renner et al*., 2014; *Rothrock et al*., 2008]. Changed surface properties, such as the increased formation of melt ponds [*Roesel and Kaleschke*, 2012], and the shift from multi-year sea ice to predominantly first-year sea ice in vast regions of the Arctic [*Maslanik et al*., 2011; *Tschudi et al*., 2010], led to increased light transmission through the sea ice in spring and summer [*Nicolaus et al*., 2012; *Perovich et al*., 2011]. Yet detailed knowledge of the physical processes governing the fate of the sea ice is limited [*Perovich and Polashenski*, 2012; *Perovich et al*., 2002], especially with regard to the role of small- to meso-scale melting processes. In the last half-century knowledge about vertical gradients of physical and biological environmental properties depended on ice cores and instruments lowered on a wire [*Frey et al*., 2011; *Grenfell*, 1977; *Light et al*., 2003; *Thomas and Dieckmann*, 2010; *Zeebe et al*., 1996], with limitations for regional upscaling. Airborne and satellite remote sensing as well as new tools for field investigations improved the study of spatially distributed processes at the ice surface [*Hudson et al*., 2012; *Perovich et al*., 1998; *Petrich et al*., 2012b], but only recently advances in the field of marine robotics allow comprehensive large scale studies underneath the polar pack ice [*Bowen et al*., 2012; *Jakuba et al*., 2008; *Kukulya et al*., 2010; *Nicolaus and Katlein*, 2013; *Williams et al*., 2013] that allow for Arctic wide upscaling [*Arndt and Nicolaus*, 2014].

One process of particular interest both for sea ice physics and biology is the partitioning of solar shortwave radiation at the sea ice surface [*Light et al*., 2008; *Perovich et al*., 2011]. In winter and spring, the snow cover

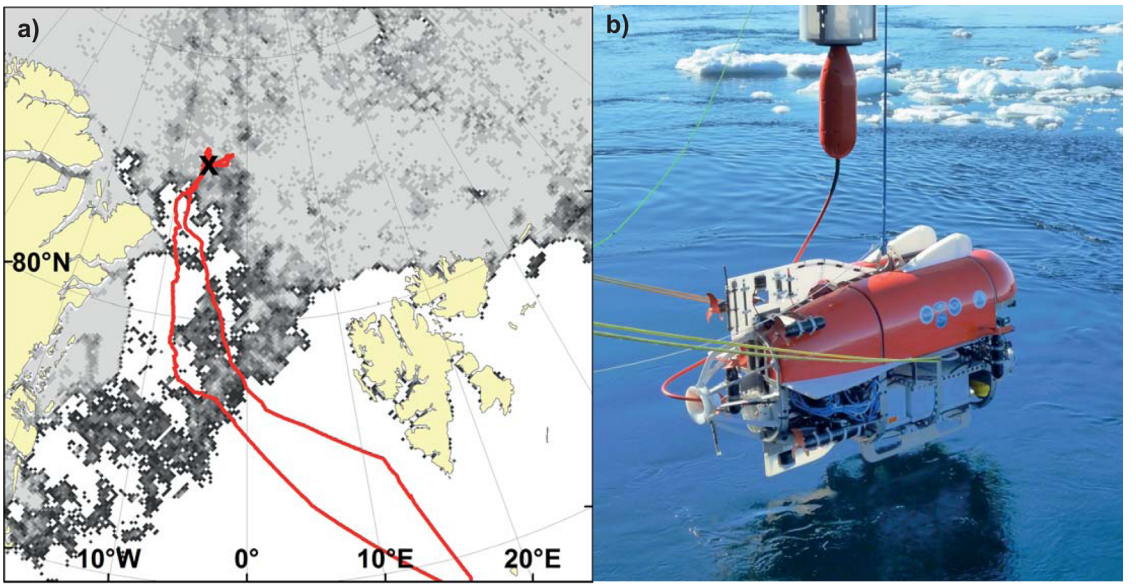

Figure 1. (a) Map showing the cruise track (red line) in the northern Fram Strait between Greenland and Spitsbergen. The black x indicates the location of the presented ice station work. Sea ice concentration of the sampling day from AMSR2 (http://www.iup.uni-bremen.de:8084/amsr2/) is shown in grey shadings with high sea ice concentration in brighter colors. (b) NUI shortly before deployment into a pool of open water on the starboard side of Polarstern. The upward looking sensors are located in the spine payload bay in between the two white landing skids toward the front of the vehicle.

on the ice limits light transmission and determines its spatial variability [*Mundy et al*., 2005]. As Arctic sea ice gets increasingly translucent over the course of the season, the fraction of the solar flux absorbed in the ice [*Nicolaus et al*., 2013a] and the water layer right beneath can sustain algal productivity and cause substantial sea ice melt. This solar heat flux can easily dominate over the ocean heat flux contribution to ice melt during summer [*Hudson et al*., 2013; *Nicolaus et al*., 2013b]. Nevertheless, shortwave radiative transfer in sea ice is often poorly represented in sea ice ocean models due to its complexity and high spatial variability on a scale smaller than the model resolution.

While the quantitative impact of the physical sea-ice properties on light transmittance is well understood for the text-book case of one-dimensional homogenous horizontal layers [*Light et al*., 2008; *Perovich*, 1996; *Perovich et al*., 1998], the influence of surface features and the three-dimensional ice-topography is poorly quantified for the pack ice of the Central Arctic where these factors vary on spatial scales of just a few meters.

The objective of this paper is to analyze the influence of the spatially varying surface properties of the sea ice cover and sea ice thickness on the spatial variability of light transmittance. The respective contribution of the two variables is assessed quantitatively on the basis of a survey conducted by the new Nereid Under-Ice (NUI) hybrid remotely operated vehicle coordinated with coregistered aerial images and classical sea ice observations. This novel approach using spatially distributed measurements overcomes the limitations of one-dimensional modeling and data analysis.

2. Methods

2.1. Sampling Site

Measurements were carried out during the expedition of the German research ice-breaker *RV Polarstern* to the Aurora mount, a hydrothermal vent site at Gakkel Ridge off Northeast Greenland (Figure 1a) [*Boetius*, 2015]. The described sea ice floe was surveyed on station PS86/080 at 82° 51′ N and 6° 19′ W on 28 July 2014 by on-site ice-thickness drillings combined with an under-ice survey of NUI and aerial images taken during a helicopter survey. Snow thickness was measured using a MagnaProbe (Snow Hydro, Fairbanks, AK, USA). During the study, air temperature was slightly below 0°C, the average sea ice drift velocity was 0.3 kn, and ice concentration was 80%.

2.2. Vehicle and Sensors

The Nereid Under Ice (NUI) vehicle (Figure 1b) is a hybrid remotely operated vehicle, designed especially for surveys in ice-covered waters [*Bowen et al*., 2012, 2014; *Jakuba et al*., 2008]. While offering the inspection

and intervention capabilities of a conventional remotely operated vehicle (ROV), the light-fiber tether concept allows the vehicle to operate in a drifting sea ice environment at increased standoff distances of in principle up to 20 km from the support vessel. In the event of failure of the light fiber-optic tether, high-bandwith optical communication to the vehicle is lost, and the vehicle enters a semi-autonomous mode in which it communicates to the ship via low-bandwidth acoustic telemetry through the water-column. In this mode the operators can send acoustic commands to the vehicle to guide it back to the ship for recovery. NUI is a recent development of the Deep Submergence Laboratory at the Woods Hole Oceanographic Institution (Woods Hole, MA, USA) in collaboration with the Johns Hopkins University (Baltimore, MD, USA). The vehicle provides space, power and communication for various payloads. Vehicle position data are determined by the navigation software via dead reckoning using a combination tracking of the ice bottom by upward-looking doppler velocity log (DVL), and ship-relative acoustic long baseline (LBL) positioning [*McFarland et al*., 2015].

Downwelling under-ice spectral irradiance and spectral zenith radiance (both 320–950 nm) were measured using two RAMSES-ACC/ARC (Trios GmbH, Rastede Germany) sensors positioned in the spine payload bay of the NUI vehicle. Here we present broadband values integrated over the 320–950 nm band after interpolation to a spectral resolution of 1 nm [*Nicolaus et al*., 2010]. The sensors were positioned approximately 0.5 m above the vehicle's depth sensor and triggered at the fastest achievable sampling rate, in most cases 0.5 Hz, leading to a spatial resolution of approximately 0.3 m during the under-ice survey. The field of view of the radiance sensor is 9.3° pointing towards zenith resulting in a mean footprint of 0.23 m at the underside of the ice varying with the sensor distance to the ice. Processing of the optical data as well as the calculation of transmittance (transflectance) as the quotient of under-ice irradiance (radiance) and the surface reference measurement has been described in *Nicolaus et al*. [2010] and *Nicolaus and Katlein* [2013]. Zenith radiance measurements were scaled with a factor 2.5 assuming isotropic scattering in the ice according to *Katlein et al*. [2014] to be comparable to irradiance measurements. Incident solar irradiance was measured with a reference sensor (RAMSES-ACC) located in the crowsnest of the ship. Due to low stratus clouds, incident light conditions exhibited very little variation and effects of shading by the ship's superstructure are negligible.

Sea-ice draft was measured as the difference between the vehicle depth and its distance to the ice bottom. The distance to the ice was measured by the upward-looking navigation DVL throughout the whole survey. During the last part of the survey, an upward-looking 260 kHz Delta T multibeam sonar (Imagenex Technology Corp., Port Coquitlam, BC, Canada) provided three-dimensional measurements of the ice bottom topography. We chose not to convert draft measurements into ice thickness, as ice thickness and draft values measured by drillings showed that the isostatic equilibrium were not valid for most single point measurements.

To register the subice data set with the aerial image and to ground-truth ice draft measurements, 6 holes of $\sim$5 cm diameter were drilled through the ice along a 90 m transect. The locations of the holes in the ice were marked with red marker paint to ease location in the aerial images. After measuring sea-ice thickness and draft with an ice-thickness gauge (Kovacs Entreprise Inc., Roseburg, OR, USA) we deployed 1 m long red-white colored marking poles hanging underneath the sea ice from ropes at $\sim$4 m depth. These poles were detectable in the 900 kHz forward looking obstacle avoidance and imaging P900 BlueView sonar (Teledyne BlueView, Bothell, WA, USA). Bearing and range from the vehicle to the closest pole were extracted from the BlueView images to establish exact positions of the poles in the coordinate system of the NUI navigation. The dead reckoning throughout the entire 2 km long trackline (Figure 2a) suffers from rotation of the ice floe and other undetermined navigation errors, so that the measurements cannot be colocated with the surface measurements. In contrast, the known position relative to the poles during the last 100 m before the survey end allows for a position accuracy of better than 1 m for this 100 m transect and thus the ability to colocate surface measurements and aerial images. The last part of the survey, conducted at a constant vehicle depth of 5 m will be referred to as the pole survey throughout the rest of this paper.

2.3. Aerial Images

Aerial images were obtained on four parallel low altitude flight lines using a downward looking GoPro digital camera (GoPro Hero 3 Black Edition, GoPro Inc., San Mateo, CA, USA) mounted to a helicopter. Images were corrected for camera distortion and merged to a photomosaic using Adobe Photoshop (Figure 2a). It was not possible to acquire higher quality images from higher altitude ($>$75 m) due to low clouds.

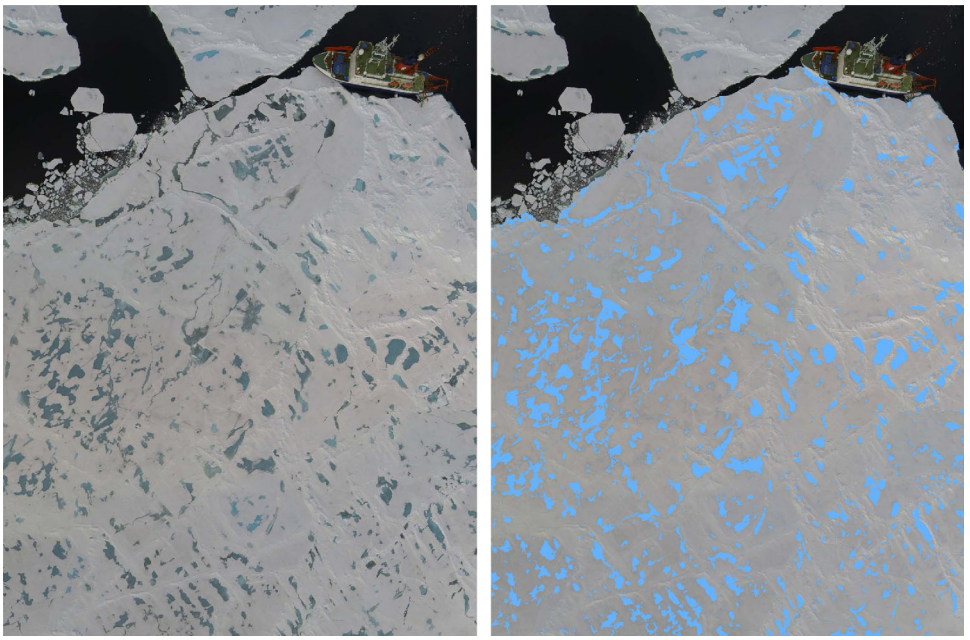

Figure 2. (a) Mosaic of aerial images of the surveyed ice floe at 82° 51′ N and 6° 19′ W acquired during a low altitude helicopter flight on 28 July 2014. The blue line indicates the estimated vehicle track underneath the ice floe, ending with the coregistered pole transect marked by the red box. The length of Polarstern as reference scale is 120 m. (b) On the same image, pixels on the surveyed floe that were classified as melt pond are marked in light blue.

Melt ponds in the image were detected using a manually drawn mask of the floe and threshold values determined from a training data set. All pixels on the floe, where $mean(R, G, B) < 70 + 0.5 \cdot B$ were classified as melt pond (Figure 2b) with R, G, B the integer values of the respective channels of the RGB color space Rec. 709 (R=700 nm, G=525 nm, B=450 nm).

To obtain a colocated aerial image, one of the images taken by the GoPro camera covering the entire area of the pole survey with least possible distortion was selected and corrected for lens distortion and vignetting. The vehicle track obtained from dead reckoning was projected to image coordinates using the marker coordinates as ground control points in a similarity transform (scale and rotate). Quantitative information about the surface conditions could thus be deduced along the vehicle track from the aerial image.

From the three RGB channels, we constructed pixel brightness by dividing the intensity (mean of R, G and B) through the maximum value of 255. This brightness value ranges between 0 and 1 and represents a proxy for surface albedo, recognizing that this study is most interested in assessing spatial variability and does not require fully calibrated albedo measurements. Extracted albedo values are similar to those generally observed on Arctic sea ice [*Perovich*, 1996] with values between 0.55 and 0.6 for melting white ice and 0.3 to 0.4 for melt-ponds. Broadband albedo values were extracted along the vehicle track, both as single pixel values and as averages over albedo values in a circle around the vehicle position with a diameter of 2 m, 4 m and 6 m. This averaging accounts for effects of lateral spreading of light by scattering in the ice as well as the large field of view of the irradiance sensor.

2.4. Analysis

From all the data available for the pole survey, we constructed a data set of simultaneous measurements of under-ice irradiance, radiance, ice draft derived from the DVL range, ice draft derived from the multibeam sonar, as well as point and spatially averaged albedo. This data set was transferred into the statistical software R to analyze the multivariate dependencies and to determine the variability explained by each variable.

To analyze the scales of spatial variability, we computed and fitted spatial variograms (Figure 4). The empirical variogram describes the variance in subsets of the data set with varying spatial distance (lag distance). Empirical variograms were fitted with exponential theoretical variograms to obtain range values. The range

parameter is defined as the lag distance at which the fitted variogram reaches ~95% of the sill value, the asymptotic variance of unrelated datapoints with large distance. Thus it describes the scale of the distance at which datapoints are related to each other.

3. Results

3.1. Physical Properties of the Ice Floe

The surveyed ice floe was of large extent (> 1 km^2) and had a modal ice draft of 1.6 m. It consisted of several parts of rather undeformed first- or second-year ice as well as heavily deformed parts. While the level ice was mostly covered by extensive melt ponds between old and young ridges, the more deformed ice also hosted isolated lighter-blue ponds (Figure 2a).

The floe surface was in an intermediate melting stage showing various stages of melt pond development. The ice surface was covered by a layer of large grains resembling wet melting snow, but also very similar to the surface scattering layer present on summer sea ice. The modal thickness of the surface layer was 8 cm. In large areas, especially adjacent to some melt ponds, the surface layer was partly saturated with water. Analysis of the aerial image revealed, that 13% of the floe was covered by melt-ponds. The length scale of melt pond variability on the floe was 9.3 m as determined by variogram analysis of the classified aerial image (range value). The thick ice, the considerable surface layer, the geographic position close to Greenland and the timing early in the melting season are the reason for the low light transmittances when compared to other studies from other regions or later in the summer [*Arrigo et al*., 2012; *Nicolaus et al*., 2012].

3.2. Pole Survey

Results from the pole survey transect are shown in Figure 3. Light transmittance was between 0.02 and 0.10 along the transect: In the vicinity of the first pole, light transmittance was high due to a melt pond, but it dropped quickly under the influence of a ridge visible on the surface. After crossing the ridge, light levels increased due to a reduction in ice draft from 2 to 1.2m before dropping again due to the thickest ice observed in the transect, between poles 2 and 3 with a draft of up to 2.5 m. The two clear peaks of light-transmittance near poles 4 and 5, respectively can be attributed to the crossing beneath two melt ponds at the surface (Figure 3a). The final increase at the end of the survey is caused by the approach to a third, larger melt pond.

A noteworthy feature of the multibeam ice draft measurements is that the under-ice topography might deviate substantially from what would be expected when looking at the surface structure. Ridges visible at the surface do not necessarily have keels visible at the underside of the ice while ice features with greater thickness do not necessarily have to be represented in the surface topography (Figure 3b). This can lead to confusion when navigating under-ice vehicles according to features visible on the surface.

Extracted albedo values lie between 0.3 and 0.6. Spatial averaging of albedo values over circles of increasing diameter shows the strength of the influence of the pond geometries on either side of the vehicle track on optical properties (Figure 3c).

Ice draft varies between 1.0 m and 2.3 m along the transect (Figure 3d). Multibeam draft data agree well with draft data acquired from the DVL when the different methods of calculation are taken into consideration. The DVL range is calculated as the average range of 4 beams angled 30° from vertical, thus averaging over an area of 1–3 m depending on the distance between instrument and ice. Comparison of the multibeam draft data with ice draft measured at the positions of the poles revealed an accuracy of <0.1 m for the ice topography, similar to what has been achieved earlier [*Wadhams et al*., 2006; *Williams et al*., 2015].

Light transmittance as observed from the irradiance and radiance sensors is clearly related to both surface albedo and ice draft. The peaks of light transmittance related to drops in the surface albedo caused by melt ponds are particularly obvious (Figures 3c and 3e).

Statistical analysis of the resulting data set reveals that 72% percent of the variance in the measured radiance can be explained by the combination of the 1 m albedo average (65%) and the ice-draft value at the spot (7%). All other combinations of the available variables described a smaller portion of the observed variance. While radiance measurements thus seem to be mostly influenced by the ice properties at the spot, irradiance measurements are influenced by albedo and ice thickness over a larger region in the vicinity of

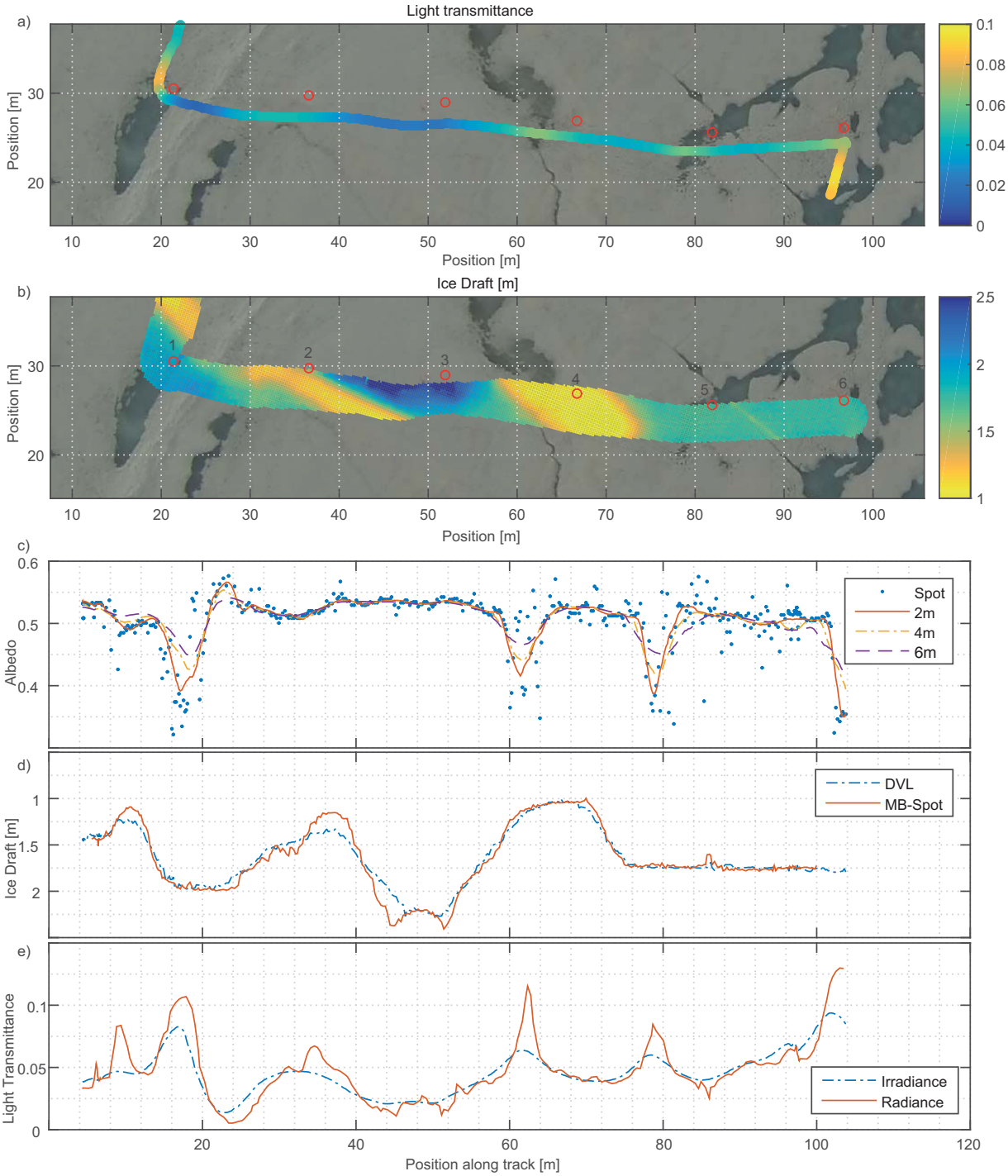

Figure 3. Physical measurements taken from the ROV during the colocated pole survey: (a) Light transmittance along the survey track. Red circles show positions of numbered marker poles. (b) Ice draft as measured along track with upward looking multibeam sonar. (c) Surface albedo extracted from the image. Blue dots indicate spot data, while lines depict data averaged over circles with different diameters. (d) Ice Draft as derived from the DVL (blue dashed line) and measured by the center beam of the multibeam sonar (red line). (e) Light transmittance measured by the radiance (red line) and irradiance (blue dashed line) sensors along the survey.

the measurement. Thus a combination of the 3 m albedo average and the draft measured from the DVL representing a spatial average of 1–3 m explains 66% percent of the variance in measured irradiance.

The contrast in peakiness between the different measured light transmission curves (Figure 3c) shows that the smooth contrasts of irradiance are mainly caused by the large sensor footprint and not by lateral light

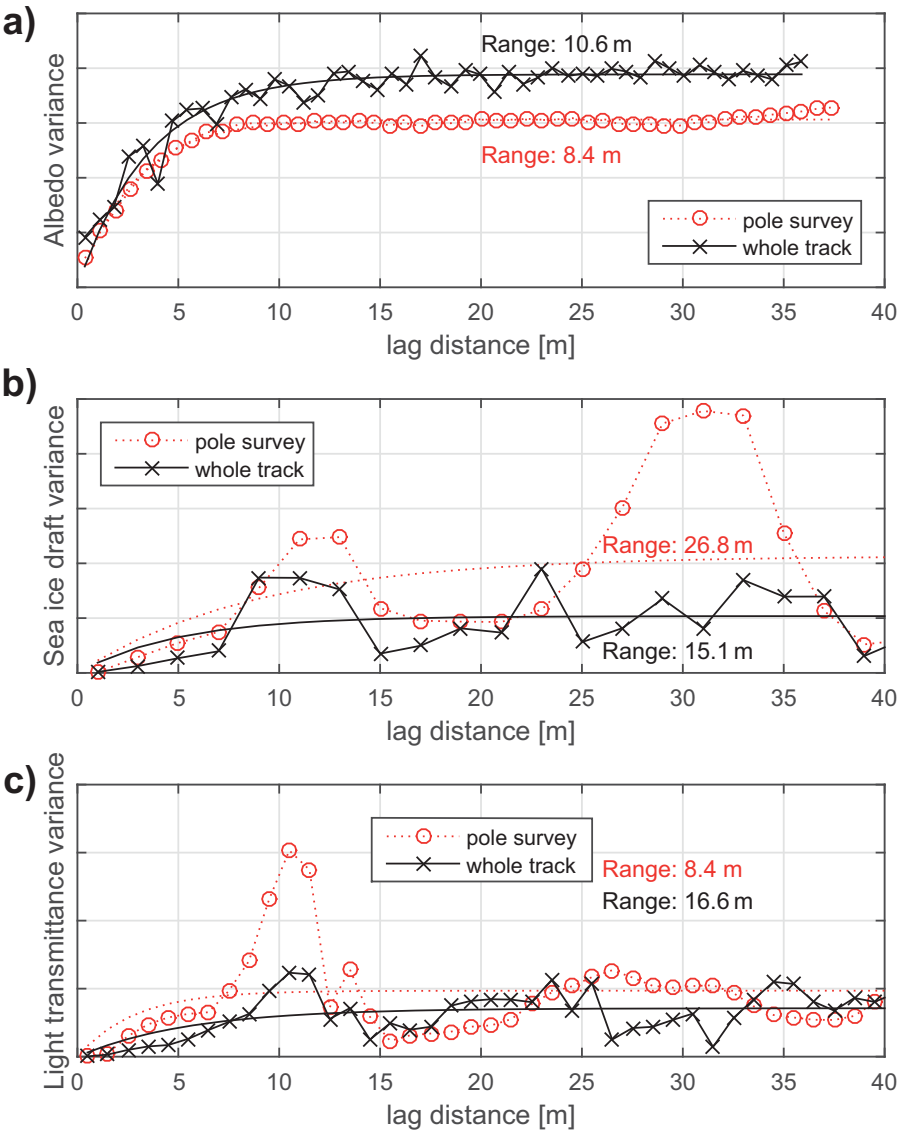

Figure 4. Variograms of (a) surface albedo, (b) sea ice draft, and (c) light transmittance. Red lines indicate variograms obtained from the area of the pole survey, while black lines are derived from all available data. Empirical variograms are shown with x as data marker, while unmarked lines are fitted theoretical exponential histograms. The range values obtained from the fitting are given as annotations in the same color as the corresponding curve. Variance is given in arbitrary units starting at zero.

propagation in the ice. If lateral light propagation were the dominant cause, then the radiance profile would be comparable in smoothness to the irradiance profile.

3.3. Scales of Spatial Variability

To investigate the length scales of the spatial variability of different variables, variograms were computed for the available data set of albedo, ice draft and light transmittance (Figure 4). The variograms were computed each for both the data set of the whole dive survey and a subset covering the pole survey only. The typical length scale of albedo variability was 10.6 m for the whole dive and 8.4 m for the pole survey. This comes from the typical size range of melt ponds which cause the highest variations in surface albedo. For sea ice draft we considered only the DVL data, as the multibeam data are not available for the entire dive. We derived length scales of ice-draft variability ranging from 15.1 m for the whole dive to 26.8 m for the pole transect. This is significantly greater than the length scale of a typical pond at this time of the year. The length scale of the variability of light transmittance was 8.4 m on the pole survey and 16.6 m when considering the whole floe, indicating different causes for the observed variability on different scales.

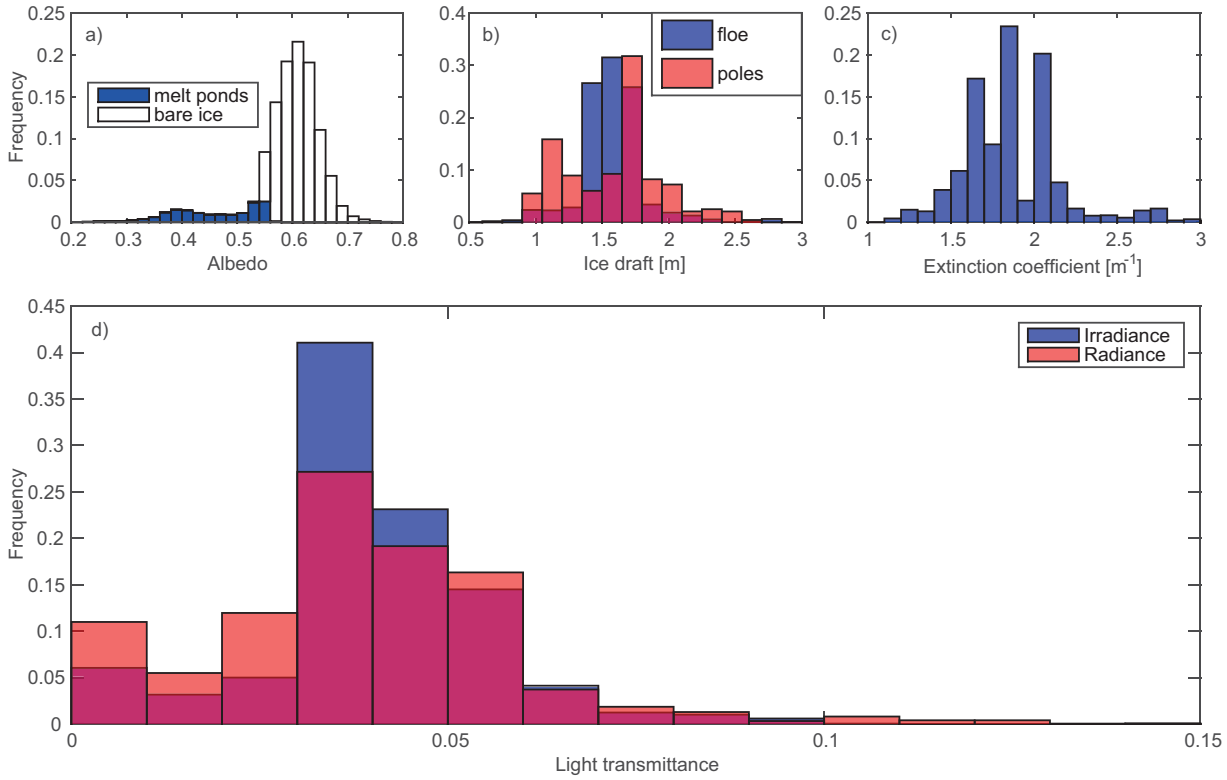

Figure 5. (a) Histogram of surface albedo derived from the aerial image. (b) Histogram of sea ice draft as measured from multibeam during the pole survey (red) and throughout the complete floe from upward looking DVL (blue). (c) Histogram of bulk broadband light extinction coefficients derived from measured light transmittance. (d) Histogram of irradiance (blue) and radiance (red, scaled to irradiance) light transmittance.

3.4. From Point Measurements to Histograms

A great advantage of spatially extensive measurements is the ability to construct histograms showing the distribution of measured values in contrast to single point values. While this technique of histograms has been used frequently for ice-thickness distributions [*Thorndike et al.*, 1975] its application to optical properties has only begun recently, triggered by the development of relevant sampling methods [*Divine et al.*, 2015; *Nicolaus et al.*, 2012, 2013a].

Figure 5a shows the frequency distribution of surface albedo pixels as derived from the aerial image. A clear bimodal distribution is visible, but the wide variety of ponds on the floe causes a wide saddle in between the two peaks related to melt ponds and bare ice respectively. Associating the albedo values with their respective surface type retrieved from color thresholding, shows that a portion of bright light blue ponds is "leaking" into the peak associated with bare sea ice.

The ice draft distribution shows differences between the two instruments related to the different sampling areas (Figure 5b). While the DVL data set covering the whole dive shows a unimodal distribution with a modal ice draft of ~1.7 m, the multibeam data covering only the pole transect shows a bimodal distribution with a consistent mode at ~1.7 m and a local mode of thinner ice at ~1.2 m.

Bulk light extinction coefficients κ computed from light transmittance T and ice draft z_i ($\kappa = -\ln\left(\frac{T}{z_d}\right)$) show a mode centered around 1.8 m^{-1} but also significantly higher values (Figure 5c). The light transmittance distribution is primarily unimodal with a modal transmittance between 0.03 and 0.04 evident from both sensors (Figure 5d). In addition, both sensors show a small secondary mode of dark patches below 0.01. Low light transmittance occurs more frequently in the radiance data as measurements at dark spots are not influenced by adjacent ponds. The tail of the distribution is longer (maximum 0.12) for the radiance sensor than for the irradiance sensor (maximum 0.09). This was expected, as small scale structures with high light transmission such as small ponds, cracks or channels are better represented by the radiance measurements.

4. Discussion

4.1. Light Transmission Under a Spatially Varying Ice Cover

Our results show that 72% of variance in the spatially varying light field underneath the ice can be explained by ice draft and surface albedo, in particular the influence of melt ponds at this time of the year when the snow cover starts to disappear. To describe the variance in the irradiance measurements best, it is necessary to use spatial averages, while the radiance field can be best described using local values. This is due to the irradiance sensor having a larger footprint than the radiance sensor.

Several factors lead to the fact that only 72% of the under-ice light field variance can be explained by surface albedo and ice draft: First, our measurements only include ice draft and not the portion of the ice above the waterline, which can have significant impact on the under ice light and is not necessarily represented in the albedo variability. Second, we were not able to quantify the spatially varying properties of the surface layer. The observed melting stage with properties in between melting snow and surface scattering layer, varied throughout the floe and included water saturation in some places. Third, lateral changes in ice internal properties caused by different stages of melt are hard to quantify. These poorly quantifiable factors can easily explain the 28% of unexplained variance in the under ice light field.

While the irradiance curve is very smooth, the radiance curve shows clearly accented peaks (Figure 3e). This shows that the smoothness of the irradiance curve is caused by measurement geometry and the large sensor footprint resulting from the sensor not being placed exactly at the ice water interface. Lateral propagation of light due to scattering in the ice is thus not the primary cause for smoothing of the irradiance curve.

Our results show that a one-dimensional approach is not enough for modeling under ice irradiance measurements as the large sensor footprint results in a significant influence of adjacent structures on the measurements. This is also the case to a lesser extent for radiance measurements, as light measured at one point immediately against the underside of the sea ice will still be influenced by optical conditions within a certain area above the point due to lateral transport of light by scattering in the ice [*Petrich et al*., 2012a; *Trodahl et al*., 1987].

4.2. Scales of Spatial Variability

Analysis of the spatial scales using variograms revealed a characteristic length scale for albedo variations around 10 m, the typical length scale of melt ponds. This is consistent with similar observations by *Petrich et al*. [2012b] on landfast ice. As noted previously by *Perovich et al*. [1998], this length scale of pond variability is closely linked to the length scale of under ice light variability due to the obvious impact of melt ponds on light transmission [*Nicolaus et al*., 2012]. We found a characteristic length scale of 8.4 m for the variance in the under ice irradiance measurements along the pole transect, which lies very close to the length scale of pond variability. Surprisingly, the characteristic length scale of under ice light variability obtained from the complete data set was 16.6 m, twice as long as the scale determined during the pole survey. This is significantly bigger than the length scale for melt ponds and lies very close to the length scale of ice draft variability observed during the whole transect of 15.1 m. Thus we suggest that the variability of under ice light is governed by variations in ice draft, when considering areas bigger than 1000 m^2. On this scale, the variability of the pond cover is averaged spatially. While the presence of ponds will only impact the mean light level, the large scale variability of under ice light is driven by changes in ice thickness which in turn also reflects the variability of ice type, its properties and the pond ratio. This result confirms the feasibility of using ice thickness as a predictor for light transmission in large-scale sea ice models during summer, when the influence of snow cover is limited.

4.3. Describing the Light-Field by Distribution Functions

Under ice data sets with large spatial extent can successfully be employed to compute histograms of ice apparent optical properties. Light transmission has proved to be related to ice draft and surface albedo, both variables for which histograms and distribution functions can be acquired using surface surveys or eventually satellite observations. We thus want to examine the possibility of composing a light transmission histogram from the distributions of surface albedo and ice draft. For reasons of simplicity we here assume that ice draft equals ice thickness, which is a good approximation for the early melting season. Different ice draft to ice thickness relations can be easily implemented analogously.

As the distributions are not completely independent from each other—e.g., ponds occur more often on thinner ice [*Fetterer and Untersteiner*, 1998; *Nicolaus et al*., 2012]—it is not possible to produce the exact light

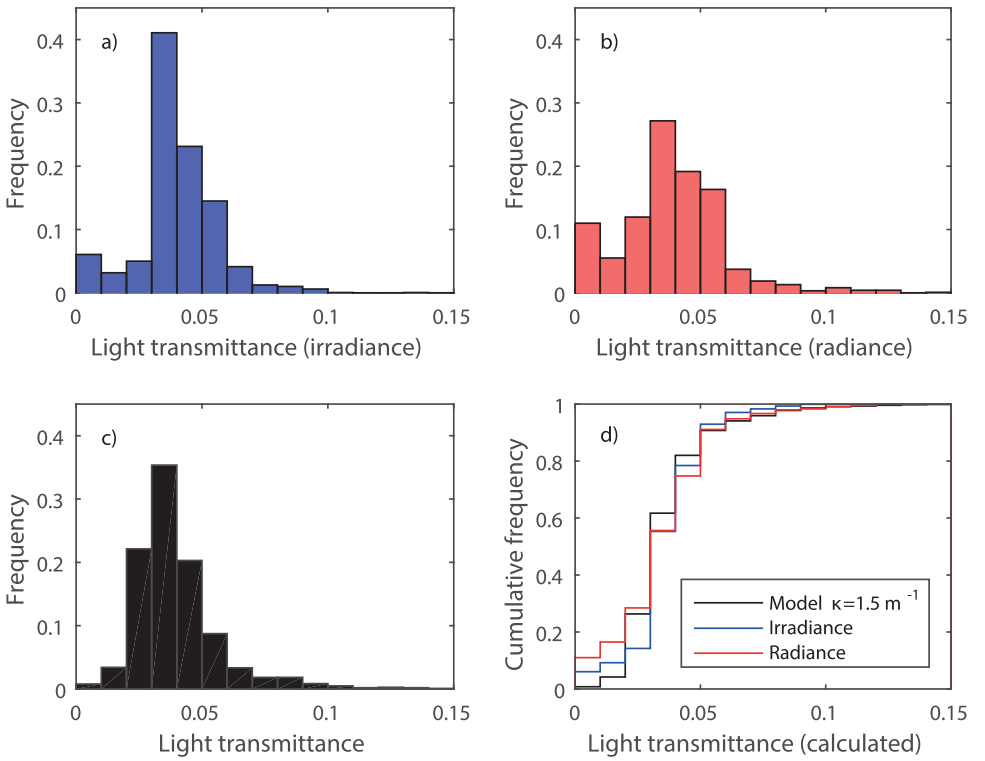

Figure 6. Histograms of light transmission as obtained from the (a) irradiance and (b) radiance sensors. (c) Light transmission histograms generated with the presented algorithm from the distribution of surface albedo and ice thickness using a extinction coefficient of $\kappa = 1.5\ \mathrm{m}^{-1}$ for the case of independent source distribution functions. (d) Same histograms presented as cumulative probability functions.

transmission histogram just out of the two distribution functions. Nevertheless, we propose a method that allows an approximation of the light transmission histogram treating the two distributions as independent or with simply constrained dependence. One argument for considering the distributions of ice draft and surface albedo to be independent is that in many cases, they will be determined by different instruments in slightly differing locations. Similarly it is extremely challenging to produce a combined data set of under ice and surface observations that are precisely colocated over a large enough area. Thus we will start with a formulation using independent distribution functions:

Let the surface albedo distribution be described by a row of albedo values $[\alpha_1, \alpha_2, \ldots, \alpha_n]$ with occurrence frequencies $[h(\alpha_1), h(\alpha_2), \ldots, h(\alpha_n)]$ complying to the normalization $\sum_{i=1}^{n} h(\alpha_i) = 1$, and the ice thickness distribution as a row of ice thickness values $[z_1, z_2, \ldots, z_m]$ with occurrence frequencies $[g(z_1), g(z_2), \ldots, g(z_m)]$ and $\sum_{i=1}^{m} g(z_i) = 1$. In a simple approach, light transmittance can be calculated from surface albedo α, ice thickness z and a known extinction coefficient κ as follows:

$$T = (1-\alpha)\exp(-\kappa z) \tag{1}$$

This equation can be evaluated for all possible combinations of n and m, yielding transmittance values $T_{1\ldots l} = [T(\alpha_1, z_1), T(\alpha_1, z_2), \ldots, T(\alpha_2, z_1), T(\alpha_2, z_2), \ \ldots, \ T(\alpha_n, z_m)]$ and combined occurrence frequencies $w_{1\ldots l} = [h(\alpha_1)\ g(z_1), h(\alpha_1)g(z_2), \ldots, h(\alpha_2)g(z_1), h(\alpha_2)g(z_2), \ \ldots, \ h(\alpha_n)g(z_m)]$ still normalized as $\sum_{i=1,j=1}^{n,m} h(\alpha_i)\, g(z_j) = 1$ with $l = nm$. Mean transmittance can now be calculated as $\bar{T} = \sum_{k=1}^{l} T_k w_k$. To acquire a meaningful histogram, these pairs of transmittance and their respective weights need to be resampled into a histogram with a large enough bin width 2λ. The histogram of transmittance occurrence frequencies is then given by:

$$f(T-\lambda \le T < T+\lambda) = \sum_{T-\lambda \le T_i < T+\lambda} w_i \tag{2}$$

As this approach realizes some unlikely combinations of albedo and ice-thickness, the total range of light transmittance may be bigger than in reality, showing a longer tail in the histogram at higher transmittances. Similarly the precision at the lower end of the calculated transmittance will be biased including unrealistic

albedo thickness combinations leading to low transmittance. Nevertheless, the respective probabilities (weights) are fairly small, so that the influence on both the mean value and the modal peak of the distribution should be negligible.

If the dependence of the ice thickness and surface albedo distribution are known or can be assumed, equation (1) will only be evaluated for the valid combinations of n and m. In this case, the resulting weights *f* need to be adjusted to comply with the normalization criterion.

This treatment can be generalized by also including other parameters. The presented parameterization proved useful for summer conditions and is expected to provide good results while melt ponds are the governing surface feature. Before melting starts, a combination of histograms of ice thickness and snow thickness might be superior to a dedicated albedo treatment as the albedo is more uniform in space. The extinction coefficient can be either included as a distribution function determined from measurements, a constant with values chosen from the literature or used as a tuning parameter depending on the purpose. For a better investigation of the general applicability of this approach, more spatially extensive data sets have to be acquired with under-ice vehicles such as NUI.

Histograms derived from our data set are shown in Figure 6. Using independent source distribution functions and an extinction coefficient of $\kappa = 1.5\ m^{-1}$ as commonly used in the literature [*Grenfell*, 1977; *Perovich*, 1996], the algorithm correctly estimates the main mode at 0.035 but slightly underestimates the occurrence of small light transmittance values (Figure 6c). As explained above, the deviations between measured and derived histogram at both ends of the distribution are expected. Comparing the cumulative distribution functions (Figure 6d) confirms a good agreement between measured and derived light transmittance distributions. While a final conclusion as to the possibility of estimating transmission histograms from distributions of ice thickness and surface albedo is not possible using this limited data set, our results encourage future exploration now that extensive spatial data sets of sea ice optics are attainable.

5. Conclusion

Our measurements conducted with a novel under ice vehicle combined with colocated surface measurements and aerial images enabled new insights into the spatial variability of the under ice light field. Measurements using irradiance sensors are strongly influenced by measurement geometry, so that under ice irradiance measurements must be analyzed in the context of ice and surface properties within a radius of several meters. This radius is determined by the distance of the sensor to the underside of the ice and lateral light propagation. The application of one-dimensional models based on spot measurements is not able to reproduce the full variability of the under ice light field.

While the spatial scales of under ice light variability are given by the scale of melt ponds when considering a smaller area ($<1000\ m^2$), the variability on larger scales is mostly driven by variations in the ice thickness. These variations may be due to ice deformation or to changes in ice type. This suggests that ice thickness might be a reliable predictor of under ice light conditions when combined with other aspects such as ice type and pond coverage.

Large spatially extensive data sets enable a statistical view on ice optical properties through the ability to construct histograms of light transmission underneath the ice. Based on our data set, we suggest an algorithm to construct a histogram of light transmittance through sea ice as a combination of distribution functions of ice thickness and surface albedo. This approach could be used to combine remote sensing data sets of ice thickness (e.g., Cryosat 2) and albedo distributions (e.g., AVHRR, MODIS) into Arctic-wide maps of light transmittance through sea ice.

Acknowledgments
We gratefully acknowledge the support of the Captain and Crew of R/V Polarstern expedition PS86. Nereid-UI development and at-sea operations were supported by the U.S. National Science Foundation Office of Polar Programs (NSF OPP ANT-1126311), National Oceanic and Atmospheric Administration Office of Exploration and Research (NOAA OER NA14OAR4320158), the Woods Hole Oceanographic Institution, the James Family Foundation, the George Frederick Jewett Foundation East. We thank Martin Steffens for providing the aerial images and the graduate school Polmar for granting an outgoing scholarship which supported the writing of this manuscript. We thank Samuel Laney for comments improving this manuscript. Additional funds supporting this work were provided to Antje Boetius by the European Research Council Advanced Investigator grant 294757. Optical data are available at http://dx.doi.org/10.1594/PANGAEA.846130 all vehicle related data are available from the Woods Hole Oceanographic Institution (mjakuba@whoi.edu). This study was funded by the Alfred-Wegener-Institut Helmholtz-Zentrum für Polar- und Meeresforschung.

References

Arndt, S., and M. Nicolaus (2014), Seasonal cycle and long-term trend of solar energy fluxes through Arctic sea ice, *Cryosphere*, *8*(6), 2219–2233, doi:10.5194/tc-8-2219-2014.

Arrigo, K. R., et al. (2012), Massive phytoplankton blooms under Arctic sea ice, *Science*, *336*(6087), 1408, doi:10.1126/science.1215065.

Boetius, A. (2015), *The Expedition PS86 of the Research Vessel POLARSTERN to the Arctic Ocean in 2014*, Alfred Wegener Inst. for Polar and Mar. Res., Bremerhaven, Germany.

Bowen, A. D., M. Jakuba, D. Yoerger, C. German, J. C. Kinsey, L. L. Whitcomb, and L. Mayer (2012), Lightly tethered unmanned underwater vehicle for under-ice exploration, Aerospace Conference, IEEE, pp. 1–12, 3–10 March, Big Sky, Mont., doi:10.1109/AERO.2012.6187038. [Available at http://ieeexplore.ieee.org/stamp/stamp.jsp?tp=&arnumber=6187038&isnumber=6186985.]

Bowen, A. D., et al. (2014), Design of Nereid-UI: A remotely operated underwater vehicle for oceanographic access under ice, Oceans - St. John's, pp. 1–6, 14–19 Sept., St. John's, NL, doi:10.1109/OCEANS.2014.7003125. [Available at http://ieeexplore.ieee.org/stamp/stamp.jsp?tp=&arnumber=7003125&isnumber=7002974.]

Divine, D. V., M. A. Granskog, S. R. Hudson, C. A. Pedersen, T. I. Karlsen, S. A. Divina, A. H. H. Renner, and S. Gerland (2015), Regional melt-pond fraction and albedo of thin Arctic first-year drift ice in late summer, *Cryosphere*, *9*(1), 255–268, doi:10.5194/tc-9-255-2015.

Fetterer, F., and N. Untersteiner (1998), Observations of melt ponds on Arctic sea ice, *J. Geophys. Res.*, *103*(C11), 24,821–24,835, doi:10.1029/98JC02034.

Frey, K. E., D. K. Perovich, and B. Light (2011), The spatial distribution of solar radiation under a melting Arctic sea ice cover, *Geophys. Res. Lett.*, *38*, L22501, doi:10.1029/2011GL049421.

Grenfell, T. C. (1977), The optical properties of ice and snow in the arctic basin, *J. Glaciol.*, *18*(80), 445–463.

Haas, C., A. Pfaffling, S. Hendricks, L. Rabenstein, J.-L. Etienne, and I. Rigor (2008), Reduced ice thickness in Arctic Transpolar Drift favors rapid ice retreat, *Geophys. Res. Lett.*, *35*, L17501, doi:10.1029/2008GL034457.

Hudson, S. R., M. A. Granskog, T. I. Karlsen, and K. Fossan (2012), An integrated platform for observing the radiation budget of sea ice at different spatial scales, *Cold Reg. Sci. Technol.*, *82*, 14–20, doi:10.1016/j.coldregions.2012.05.002.

Hudson, S. R., M. A. Granskog, A. Sundfjord, A. Randelhoff, A. H. H. Renner, and D. V. Divine (2013), Energy budget of first-year Arctic sea ice in advanced stages of melt, *Geophys. Res. Lett.*, *40*, 2679–2683, doi:10.1002/grl.50517.

Jakuba, M. V., L. L. Whitcomb, D. R. Yoerger, and A. D. Bowen (2008), Toward under-ice operations with hybrid underwater robotic vehicles, AUV 2008, IEEE/OES, pp. 1, 9, 13–14 Oct., Woods Hole, Mass., doi:10.1109/AUV.2008.5347599. [Available at http://ieeexplore.ieee.org/stamp/stamp.jsp?tp=&arnumber=5347599&isnumber=5290522.]

Katlein, C., M. Nicolaus, and C. Petrich (2014), The anisotropic scattering coefficient of sea ice, *J. Geophys. Res. Oceans*, *119*, 842–855, doi:10.1002/2013JC009502.

Kukulya, A., et al. (2010), Under-ice operations with a REMUS-100 AUV in the Arctic, Autonomous Underwater Vehicles (AUV), IEEE/OES, pp. 1, 8, 1–3 Sept., Monterey, Calif., doi:10.1109/AUV.2010.5779661. [Available at http://ieeexplore.ieee.org/stamp/stamp.jsp?tp=&arnumber=5779661&isnumber=5779639.]

Kwok, R., and D. A. Rothrock (2009), Decline in Arctic sea ice thickness from submarine and ICESat records: 1958–2008, *Geophys. Res. Lett.*, *36*, L15501, doi:10.1029/2009GL039035.

Light, B., G. A. Maykut, and T. C. Grenfell (2003), A two-dimensional Monte Carlo model of radiative transfer in sea ice, *J. Geophys. Res.*, *108*(C7), 3219, doi:10.1029/2002JC001513.

Light, B., T. C. Grenfell, and D. K. Perovich (2008), Transmission and absorption of solar radiation by Arctic sea ice during the melt season, *J. Geophys. Res.*, *113*, C03023, doi:10.1029/2006JC003977.

Maslanik, J. A., J. Stroeve, C. Fowler, and W. Emery (2011), Distribution and trends in Arctic sea ice age through spring 2011, *Geophys. Res. Lett.*, *38*, L13502, doi:10.1029/2011GL047735.

McFarland, C., M. V. Jakuba, S. Suman, J. C. Kinsey, and L. L. Whitcomb (2015), Toward ice-relative navigation of underwater robotic vehicles under moving sea-ice: Experimental evaluation in the Arctic Sea, Robotics and Automation (ICRA), IEEE International Conference on, pp. 1527–1534, 26–30 May, Seattle, Wash., doi:10.1109/ICRA.2015.7139392. [Available at http://ieeexplore.ieee.org/stamp/stamp.jsp?tp=&arnumber=7139392&isnumber=7138973.]

Meier, W. N., et al. (2014), Arctic sea ice in transformation: A review of recent observed changes and impacts on biology and human activity, *Rev. Geophys.*, *52*, 185–217, doi:10.1002/2013RG000431.

Mundy, C. J., D. G. Barber, and C. Michel (2005), Variability of snow and ice thermal, physical and optical properties pertinent to sea ice algae biomass during spring, *J. Mar. Syst.*, *58*(3-4), 107–120, doi:10.1016/j.jmarsys.2005.07.003.

Nicolaus, M., and C. Katlein (2013), Mapping radiation transfer through sea ice using a remotely operated vehicle (ROV), *Cryosphere*, *7*(3), 763–777, doi:10.5194/tc-7-763-2013.

Nicolaus, M., S. R. Hudson, S. Gerland, and K. Munderloh (2010), A modern concept for autonomous and continuous measurements of spectral albedo and transmittance of sea ice, *Cold Reg. Sci. Technol.*, *62*(1), 14–28, doi:10.1016/j.coldregions.2010.03.001.

Nicolaus, M., C. Katlein, J. Maslanik, and S. Hendricks (2012), Changes in Arctic sea ice result in increasing light transmittance and absorption, *Geophys. Res. Lett.*, *39*, L24501, doi:10.1029/2012GL053738.

Nicolaus, M., C. Petrich, S. R. Hudson, and M. A. Granskog (2013a), Variability of light transmission through Arctic land-fast sea ice during spring, *Cryosphere*, *6*(5), 4363–4385, doi:10.5194/tcd-6-4363-2012.

Nicolaus, M., S. Arndt, C. Katlein, J. Maslanik, and S. Hendricks (2013b), Correction to "Changes in Arctic sea ice result in increasing light transmittance and absorption," *Geophys. Res. Lett.*, *40*, 2699–2700, doi:10.1002/grl.50523.

Perovich, D. K. (1996), The optical properties of sea ice, *Monogr. 96-1*, U.S. Army Cold Regions Research and Engineering Laboratory, Hanover, N. H.

Perovich, D. K. (2011), The changing Arctic sea ice cover, *Oceanography*, *24*(3), 162–173.

Perovich, D. K., and C. Polashenski (2012), Albedo evolution of seasonal Arctic sea ice, *Geophys. Res. Lett.*, *39*, L08501, doi:10.1029/2012GL051432.

Perovich, D. K., C. S. Roesler, and W. S. Pegau (1998), Variability in Arctic sea ice optical properties, *J. Geophys. Res.*, *103*(C1), 1193–1208, doi:10.1029/97JC01614.

Perovich, D. K., T. C. Grenfell, B. Light, and P. V. Hobbs (2002), Seasonal evolution of the albedo of multiyear Arctic sea ice, *J. Geophys. Res.*, *107*(C10), 8044, doi:10.1029/2000JC000438.

Perovich, D. K., K. F. Jones, B. Light, H. Eicken, T. Markus, J. Stroeve, and R. Lindsay (2011), Solar partitioning in a changing Arctic sea-ice cover, *Ann. Glaciol.*, *52*(57), 192–196.

Petrich, C., M. Nicolaus, and R. Gradinger (2012a), Sensitivity of the light field under sea ice to spatially inhomogeneous optical properties and incident light assessed with three-dimensional Monte Carlo radiative transfer simulations, *Cold Reg. Sci. Technol.*, *73*, 1–11, doi:10.1016/j.coldregions.2011.12.004.

Petrich, C., H. Eicken, C. M. Polashenski, M. Sturm, J. P. Harbeck, D. K. Perovich, and D. C. Finnegan (2012b), Snow dunes: A controlling factor of melt pond distribution on Arctic sea ice, *J. Geophys. Res.*, *117*, C09029, doi:10.1029/2012JC008192.

Renner, A. H. H., S. Gerland, C. Haas, G. Spreen, J. F. Beckers, E. Hansen, M. Nicolaus, and H. Goodwin (2014), Evidence of Arctic sea ice thinning from direct observations, *Geophys. Res. Lett.*, *41*, 5029–5036, doi:10.1002/2014GL060369.

Roesel, A., and L. Kaleschke (2012), Exceptional melt pond occurrence in the years 2007 and 2011 on the Arctic sea ice revealed from MODIS satellite data, *J. Geophys. Res.*, *117*, C05018, doi:10.1029/2011JC007869.

Rothrock, D. A., D. B. Percival, and M. Wensnahan (2008), The decline in arctic sea-ice thickness: Separating the spatial, annual, and interannual variability in a quarter century of submarine data, *J. Geophys. Res.*, *113*, C05003, doi:10.1029/2007JC004252.

Serreze, M. C., M. M. Holland, and J. Stroeve (2007), Perspectives on the Arctic's shrinking sea-ice cover, *Science*, *315*(5818), 1533–1536, doi: 10.1126/science.1139426.

Stroeve, J. C., M. M. Holland, W. Meier, T. Scambos, and M. Serreze (2007), Arctic sea ice decline: Faster than forecast, *Geophys. Res. Lett.*, *34*, L09501, doi:10.1029/2007GL029703.

Stroeve, J. C., M. C. Serreze, M. M. Holland, J. E. Kay, J. Malanik, and A. P. Barrett (2012), The Arctic's rapidly shrinking sea ice cover: A research synthesis, *Clim. Change*, *110*(3-4), 1005–1027, doi:10.1007/s10584-011-0101-1.

Thomas, N. D., and G. S. Dieckmann (2010), *Sea Ice*, John Wiley, West Sussex, U. K. [Available at http://eu.wiley.com/WileyCDA/WileyTitle/productCd-1405185805.html.]

Thorndike, A. S., D. A. Rothrock, G. A. Maykut, and R. Colony (1975), The thickness distribution of sea ice, *J. Geophys. Res.*, *80*(33), 4501–4513, doi:10.1029/JC080i033p04501.

Trodahl, H. J., R. G. Buckley, and S. Brown (1987), Diffusive transport of light in sea ice, *Appl. Opt.*, *26*(15), 3005–3011, doi:10.1364/AO.26.003005.

Tschudi, M., C. Fowler, J. Maslanik, and J. Stroeve (2010), Tracking the Movement and Changing Surface Characteristics of Arctic Sea Ice, *IEEE J-Stars*, *3*(4), 536–540, doi:10.1109/Jstars.2010.2048305.

Wadhams, P., J. P. Wilkinson, and S. D. McPhail (2006), A new view of the underside of Arctic sea ice, *Geophys. Res. Lett.*, *33*, L04501, doi: 10.1029/2005GL025131.

Williams, G. D., et al. (2013), Beyond point measurements: Sea ice floes characterized in 3-D, *Eos Trans. AGU*, *94*(7), 69–70, doi:10.1002/2013EO070002.

Williams, G. D., T. Maksym, J. Wilkinson, C. Kunz, C. Murphy, P. Kimball, and H. Singh (2015), Thick and deformed Antarctic sea ice mapped with autonomous underwater vehicles, *Nat. Geosci.*, *8*(1), 61–67, doi: 10.1038/ngeo2299.

Zeebe, R. E., H. Eicken, D. H. Robinson, D. WolfGladrow, and G. S. Dieckmann (1996), Modeling the heating and melting of sea ice through light absorption by microalgae, *J. Geophys. Res.*, *101*(C1), 1163–1181, doi:10.1029/95JC02687.